






Shahid Chamran
University of Ahvaz

Journal of Applied and Computational Mechanics



Research Paper

Local Thermal Non-equilibrium Analysis of Cu-Al₂O₃ Hybrid Nanofluid Natural Convection in a Partially Layered Porous Enclosure with Wavy Walls

Hakim T. Kadhim^{1,2}, Zaid M. Al Dulaimi¹, Aldo Rona²

¹ Mechanical Department, Al-Furat Al-Awsat Technical University, Kufa, 54002, Iraq, Emails: dw.hkm@atu.edu.iq, hk239@le.ac.uk (H.T.K), dulaimizm@atu.edu.iq (Z.M.D)

² School of Engineering, University of Leicester, LE1 7RH, United Kingdom, Email: aldo.rona@leicester.ac.uk

Received October 04 2022; Revised November 24 2022; Accepted for publication December 12 2022.

Corresponding author: H.T. Kadhim (dw.hkm@atu.edu.iq)

© 2022 Published by Shahid Chamran University of Ahvaz

Abstract. A numerical study is performed to investigate the local thermal non-equilibrium effects on the natural convection in a two-dimensional enclosure with horizontal wavy walls, layered by a porous medium, saturated by Cu-Al₂O₃/water hybrid nanofluid. It is examined the influence of the nanoparticle volume fraction, varied from 0 to 0.04, the Darcy number ($10^{-5} \leq Da \leq 10^{-2}$), the modified conductivity ratio ($0.1 \leq \gamma \leq 1000$), the porous layer height ($0 \leq H_p \leq 1$), and the wavy wall wavenumber ($1 \leq N \leq 5$) on natural convection in the enclosure. Predictions of the steady incompressible flow and temperature fields are obtained by the Galerkin finite element method, using the Darcy-Brinkman model in the porous layer. These are validated against previous numerical and experimental studies. By resolving separately the temperature fields of the working fluid and of the porous matrix, the local thermal non-equilibrium model exposed hot and cold spot formation and mitigation mechanisms on the heated and cooled walls. By determining the convection cell strength, the Darcy number is the first rank controlling parameter on the heat transfer performance, followed by N , H_p and γ . The heat transfer rate through the hybrid nanofluid and solid phases is highest when $N = 4$ at a fixed value of nanoparticle volume fraction.

Keywords: Hybrid nanofluid; Thermal non-equilibrium model; Natural convection; Corrugated cavity; Porous layer.

1. Introduction

Natural (free) convection plays an important role in determining the rate of heat transfer through enclosures fully or partially filled with a porous medium. Among these, enclosures with wavy or corrugated walls draw a special interest, as these walls can enhance the heat exchange rate compared to flat walls. Understanding and selecting appropriate design parameters for wavy cavities can deliver heat transfer performance advantages in a range of practical applications. These include electronic packages, micro-electronic devices, the cooling of transpiration, the management of nuclear waste, building thermal insulators, grain storage and geothermal power plants [1-4]. Whilst wavy cavities are in use, limited work has been reported in previous studies compared to the classical square cavity and to inclined and rectangular walls geometries. This is because the wavy geometries are more complex [5-7], which results in an increased the number of parameters to be studied and in more demanding numerical model. Modelling wavy geometries has the potential to provide attractive rewards, such as growing the knowledge of the flow physics and of the heat transport and thermal performance, thus enabling more performing engineering applications.

In certain applications, inserting a porous layer in a cavity filled with either pure fluid or nanofluid can enhance the overall heat transfer rate across it. The porous medium dissipates the flow kinetic energy reducing the convected heat, however, heat conduction through the porous medium compensates this effect, resulting in a net heat transfer gain. Increasing the Darcy number, which describes the permeability of the porous medium, can decrease the resistance to the flow motion in natural convection cells generated in the porous medium. In enclosures partially layered by a porous medium, the porous media can be orientated either vertically [8, 9] or horizontally [10, 11], utilizing either a permeable or an impermeable interface. Kasaeian and Daneshazarian [12] reviewed a range of studies on such geometries, with different nanofluids in porous media, boundary conditions, and flow regimes, collating the overall heat transfer performance. Miroschnichenko and Sheremet [13] investigated numerically the flow and heat transfer of Al₂O₃/water nanofluid in an enclosure consisting of two layers of plain fluid and two layers of porous media. The results showed that increasing the height of the porous layers significantly enhances the convective heat transfer through the enclosure.

A number of heat convection numerical investigations on porous media [14-21] assumed the temperature of the porous matrix equal to that of the fluid inside it. This Local Thermal Equilibrium (LTE) assumption weakens as the temperature difference between the solid matrix and the fluid within it increases, which creates Local Thermal Non-Equilibrium (LTNE). This prompted to numerically investigate enclosures entirely or partially filled with porous media under LTNE assumptions. LTNE



underpins several important engineering applications, such as the cooling of electronic components and solar energy collectors [22]. Alsabery et al. [23] studied numerically the free convection inside a square enclosure with vertical corrugated walls filled by constant thickness layers of porous material, saturated with Alumina nanoparticle water-based nanofluid. The results showed that the heat transfer rates of the solid and nanofluid phases increase as the porosity rises, at increasing Darcy numbers. Izadi, Hoghoughi et al. [24] used the Buongiorno LTNE model to investigate the free convection in an enclosure filled by a porous medium, saturated by nanofluid, heated by a single pipe running through it, and cooled at its wavy side walls. The authors showed the benefit of using this LTNE model where a large convection heat transfer coefficient is present at the interface between the nanofluid and the permeable solid.

Another effective way to significantly enhance the convection heat transfer inside a cavity is by adding a combination of metallic and non-metallic nanoparticles to the baseline pure fluid, thereby generating a "hybrid nanofluid" [25-28]. The hybrid nanofluid benefits from the properties of both particle types. Chamkha et al. [29] modelled by finite elements, under LTNE assumptions, the natural convective heat transfer of Copper-Alumina hybrid nanofluids in a square cavity with a solid block adjacent to a porous block at the base, covered by a layer of clear fluid. The findings indicated that the increase in the thickness of the porous-solid layer reduces the rate of the heat transfer due to the reduction in the circulation of the hybrid nanofluid. Ghalambaz et al. [30] performed a conjugate heat transfer simulation, under LTNE conditions, of the free convection of Ag-MgO hybrid nanofluid in a porous square enclosure. The results showed that employing the hybrid nanoparticles increases the heat transfer rate and decreases the flow strength inside the enclosure, compared to pure water. Alsabery et al. [31] examined the mixed convection heat transfer in a lid-driven enclosure with wavy side walls kept at different temperatures, enclosing a solid square prism submerged in hybrid nanofluid. These authors studied the effects of the Richardson number, the nanoparticle volume fraction, the wavy wall wavenumber, and the relative position and side length of the prism. The results showed that locating the prism in the middle of the cavity enhances the heat transfer rate. Other natural convection configurations that use hybrid nanofluids are documented in the literature [32-39].

In this study, a numerical analysis is performed on the convective heat transfer through an enclosure featuring sinusoidal corrugations in its constant temperature floor and adiabatic ceiling, partially filled with a horizontal porous layer, saturated with Cu-Al₂O₃/water hybrid nanofluid. Heat transfer is driven by the constant temperature difference between the straight side walls and the floor. The Local Thermal Non-Equilibrium (LTNE) effects on the flow field and heat transfer rate are examined for various configurations of the wavy enclosure. To the authors' best knowledge, no work has been reported to date on the LTNE effects in a composite corrugated enclosure with a porous layer filled by hybrid nanofluid. In addition, this work evaluates the heat transfer performance gain using a hybrid nanofluid (Cu-Al₂O₃/water) compared to a regular nanofluid (Al₂O₃/water). As a result, this work makes a new contribution to current and future industrial applications of hybrid nanofluid technology.

2. Numerical Model

2.1 Description of the enclosure

Consider a corrugated enclosure partially filled with two layers of Cu-Al₂O₃/water hybrid nanofluid and a porous medium saturated with the hybrid nanofluid. Figure 1 shows a two-dimensional schematic diagram of the physical model of the wavy enclosure having the dimensions ($L \times L$). A specific case is shown in Fig. 1, in which half of the cavity is filled with porous medium. The wavy bottom wall of the enclosure is held at a constant hot temperature T_h while the left and right vertical sidewalls are at a constant cold temperature T_c . The upper wavy wall is thermally insulated. The interface boundary between the hybrid nanofluid layer and the porous layer is permeable. A constant amplitude A of 10% is used for the wavy profile of the horizontal walls of the enclosure. For the top wall $y_{wall} = L - A \sin(N\pi x/L)$ and for the bottom wall $y_{wall} = -A \sin(N\pi x/L)$, where $N = 2$ in Fig. 1. This is also used in [40] and recommended in [41] to prevent generating secondary vortices near the wavy walls, particularly with increasing the number of undulation. This study assumes that the hybrid nanofluid is an incompressible, laminar, and homogeneous combination of water-based fluid having Cu and Al₂O₃ nanoparticles. Table 1 illustrates the physical properties of the Cu-Al₂O₃ hybrid nanofluid in which no variations in these properties is assumed, except for the density within the buoyancy term of equation (3), which is evaluated using the Boussinesq approximation. A Newtonian behaviour of the Cu-Al₂O₃/water hybrid nanofluid is assumed [42]. In the Darcy number, the permeability value is calculated assuming a constant porosity, or void fraction, $\varepsilon = 0.398$ that is evaluated according to [43]. Specifically, the permeability $K = \varepsilon^2 d_m^2 / [150(1 - \varepsilon)^2]$, where d_m is the mean particle size of the porous medium.

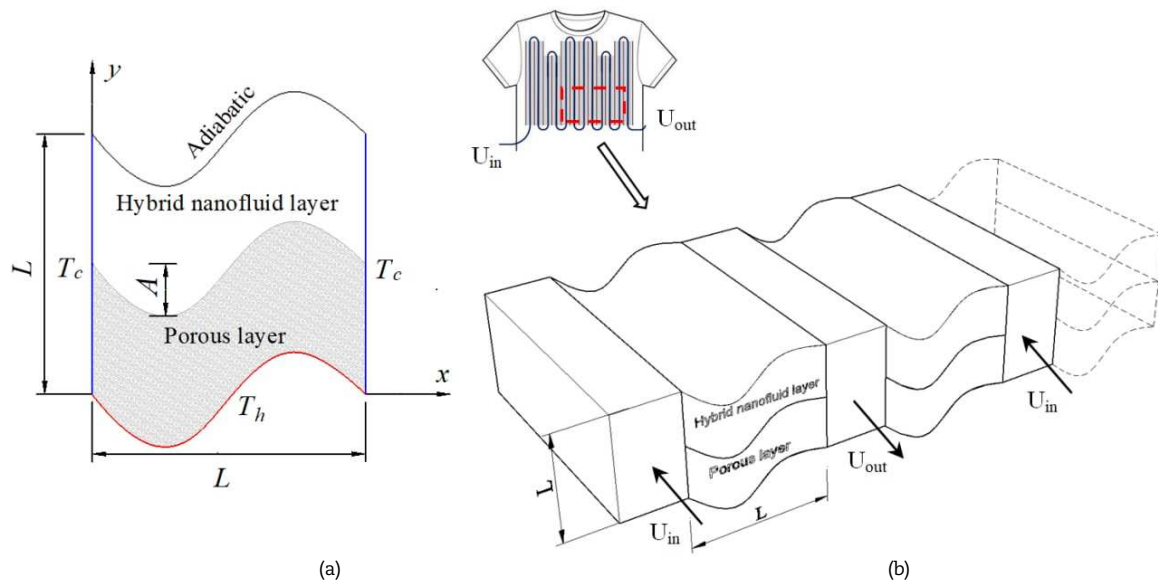


Fig. 1. (a) Schematic representation of the hybrid superposed wavy porous layers, (b) isometric view of the cut-out from a liquid cooled vest.



Table 1. Thermophysical characteristics of the hybrid nanofluid constituents [50].

Physical properties	Water	Cu	Al ₂ O ₃
C_p (J kg ⁻¹ K ⁻¹)	4179	385	765
ρ (kg m ⁻³)	997.1	8933	3970
k (W m ⁻¹ K ⁻¹)	0.613	401	40
β (K ⁻¹)	21×10^{-5}	1.67×10^{-5}	0.85×10^{-5}

Figure 1(b) illustrates a possible practical implementation of the convection cell sketched in Figure 1(a). High performance athletes, such as race car pilots and pilots of high-performance aircraft use a liquid cooled vest for managing the body temperature. The convection cell could be woven into the fabric of a liquid cooled vest to enhance the heat transfer rate from the fabric, which is in contact with the skin, to the liquid coolant channels.

2.2 Governing equations

The mass and heat transport through the enclosure defined in section 2.1 are evaluated based on the conservation of mass, linear momentum, and energy. A conjugate heat and mass transfer problem is solved across the interface between the fluid in the hybrid nanofluid layer and the fluid and solid in the porous layer [44]. Inside the composite hybrid nanofluid porous layer, the LTNE model given in [45] is used. This results in the following set of dimensionless governing equations:

For the hybrid nanofluid layer:

$$\frac{\partial U_{hnf}}{\partial X} + \frac{\partial V_{hnf}}{\partial Y} = 0 \quad (1)$$

$$U_{hnf} \frac{\partial U_{hnf}}{\partial X} + V_{hnf} \frac{\partial U_{hnf}}{\partial Y} = -\frac{\partial P}{\partial X} + \frac{\rho_{bf}}{\rho_{hnf}(1-\phi)^{2.5}} \times Pr \times \left(\frac{\partial^2 U_{hnf}}{\partial X^2} + \frac{\partial^2 U_{hnf}}{\partial Y^2} \right) \quad (2)$$

$$U_{hnf} \frac{\partial V_{hnf}}{\partial X} + V_{hnf} \frac{\partial V_{hnf}}{\partial Y} = -\frac{\partial P}{\partial Y} + \frac{\rho_{bf}}{\rho_{hnf}(1-\phi)^{2.5}} \times Pr \times \left(\frac{\partial^2 V_{hnf}}{\partial X^2} + \frac{\partial^2 V_{hnf}}{\partial Y^2} \right) + \frac{(\rho\beta)_{hnf}}{\rho_{hnf}\beta_{bf}} \times Pr.Ra.\theta_{hnf} \quad (3)$$

$$U_{hnf} \frac{\partial \theta_{hnf}}{\partial X} + V_{hnf} \frac{\partial \theta_{hnf}}{\partial Y} = \frac{\alpha_{hnf}}{\alpha_{bf}} \left(\frac{\partial^2 \theta_{hnf}}{\partial X^2} + \frac{\partial^2 \theta_{hnf}}{\partial Y^2} \right) \quad (4)$$

For the porous/hybrid nanofluid layer:

$$\frac{\partial U_{hnf}}{\partial X} + \frac{\partial V_{hnf}}{\partial Y} = 0 \quad (5)$$

$$U_{hnf} \frac{\partial U_{hnf}}{\partial X} + V_{hnf} \frac{\partial U_{hnf}}{\partial Y} = -\frac{\partial P}{\partial X} + \frac{\rho_{bf}}{\rho_{hnf}(1-\phi)^{2.5}} \times Pr \times \left(\frac{\partial^2 U_{hnf}}{\partial X^2} + \frac{\partial^2 U_{hnf}}{\partial Y^2} \right) - \frac{\rho_{bf}}{\rho_{hnf}(1-\phi)^{2.5}} \times U_{hnf} \frac{Pr}{Da} \quad (6)$$

$$U_{hnf} \frac{\partial V_{hnf}}{\partial X} + V_{hnf} \frac{\partial V_{hnf}}{\partial Y} = -\frac{\partial P}{\partial Y} + \frac{\rho_{bf}}{\rho_{hnf}(1-\phi)^{2.5}} Pr \times \left(\frac{\partial^2 V_{hnf}}{\partial X^2} + \frac{\partial^2 V_{hnf}}{\partial Y^2} \right) + \frac{(\rho\beta)_{hnf}}{\rho_{hnf}\beta_{bf}} \times Pr.Ra.\theta_{hnf} - \frac{\rho_{bf}}{\rho_{hnf}(1-\phi)^{2.5}} \times V_{hnf} \frac{Pr}{Da} \quad (7)$$

$$U_{hnf} \frac{\partial \theta_{hnf}}{\partial X} + V_{hnf} \frac{\partial \theta_{hnf}}{\partial Y} = \frac{\alpha_{hnf}}{\alpha_{bf}} \left[\left(\frac{\partial^2 \theta_{hnf}}{\partial X^2} + \frac{\partial^2 \theta_{hnf}}{\partial Y^2} \right) + H \times (\theta_p - \theta_{hnf}) \right] \quad (8)$$

$$\frac{\partial^2 \theta_p}{\partial X^2} + \frac{\partial^2 \theta_p}{\partial Y^2} = \gamma \times H \times (\theta_{hnf} - \theta_p) \quad (9)$$

The following non-dimensional variables are used in equations (1) to (9):

$$X = \frac{x}{L}, \quad Y = \frac{y}{L}, \quad U = \frac{uL}{\alpha_{bf}}, \quad V = \frac{vL}{\alpha_{bf}}, \quad P = \frac{pL^2}{\rho_{bf}\alpha_{bf}^2}, \quad Pr = \frac{\rho_{bf}}{\alpha_{bf}}, \quad \theta_{hnf} = \frac{T_{hnf} - T_c}{T_h - T_c}, \quad \theta_p = \frac{T_p - T_c}{T_h - T_c},$$

$$Ra = \frac{\beta.g.\Delta T.L^3}{\rho_{bf}.\alpha_{bf}}, \quad Da = \frac{K}{L^2}, \quad H = \frac{hL^2}{k_{hnf}}, \quad \gamma = \frac{k_{hnf}}{(1-\epsilon)k_p}$$

The local and average Nusselt numbers are obtained along the bottom wavy wall of the enclosure (the heated wall of Fig. 1) using the relations [46]:

$$Nu_{Local} = -\frac{k_{hnfs}}{k_{bf}} \frac{\partial \theta}{\partial n} \quad (10)$$

where k_{hnfs} represents k_{hnf} for the hybrid nanofluid phase and k_s for the solid phase, and:

$$Nu_{av} = \int_0^1 Nu_{Local} ds \quad (11)$$



where $\theta = (T - T_c) / (T_h - T_c)$ is the dimensionless temperature, n is the inward normal direction of the wavy wall, and s is the dimensionless arc length distance along the wavy wall, such that $0 \leq s \leq 1$, over $0 \leq X \leq 1$.

The strength of the free convection in the cavity is determined based on a potential flow representation of the fluid motion [47], by which:

$$\frac{\partial^2 \Psi}{\partial X^2} + \frac{\partial^2 \Psi}{\partial Y^2} = \frac{\partial U}{\partial Y} - \frac{\partial V}{\partial X} \tag{12}$$

The clockwise and anticlockwise flow directions are marked by the negative and positive signs of the streamfunction Ψ , respectively.

2.3 Boundary conditions

The following boundary conditions are applied on the bounding surfaces of the computational domain of Fig. 1:

- Along the heated bottom wavy wall of the enclosure denoted by T_h in Fig. 1: $U = V = 0$, $\theta_{hnf} = \theta_p = 1$.
- Along the cold left and right walls of the enclosure denoted by T_c in Fig. 1: $U = V = 0$, $\theta_{hnf} = \theta_p = 0$.
- Along the adiabatic top wall of the enclosure: $U = V = 0$, $\partial\theta / \partial n = 0$.
- Along the interface between the layer of hybrid nanofluid and the layer of porous medium: θ_{hnf}^+ , θ_{hnf}^- , $\Psi^+ = \Psi^-$, and $\partial\theta / \partial n = \partial\theta_{hnf}^+ / K_r \partial n$.

where K_r evaluates the thermal conductivity ratio between the porous region and the hybrid nanofluid region and superscripts + and - indicate conditions just above and just below the wavy interface.

At the corner between the bottom wavy wall and the side walls, $U = V = 0$ and $\theta_{hnf} = \theta_p = 0.5$. The weak form implementation of the conservative laws in the discontinuous Galerkin setting provides a finite temperature gradient and hence a finite heat transfer rate at these corners.

2.4 Thermophysical characteristics of the Cu-Al₂O₃ hybrid nanofluid

The thermophysical characteristics of the Cu-Al₂O₃/water hybrid nanofluid can be evaluated by weighted mass averaging the corresponding properties of its molecular constituents [48, 49].

The density of the hybrid nanofluid is defined as:

$$\rho_{hnf} = \phi_{Al_2O_3} \rho_{Al_2O_3} + \phi_{Cu} \rho_{Cu} + (1 - \phi) \rho_{bf} \tag{13}$$

where $\phi = \phi_{Al_2O_3} + \phi_{Cu}$ is the hybrid nanoparticles combined volume fraction and:

$$(\rho C_p)_{hnf} = \phi_{Al_2O_3} (\rho C_p)_{Al_2O_3} + \phi_{Cu} (\rho C_p)_{Cu} + (\rho C_p)_{bf} (1 - \phi) \tag{14}$$

The thermal expansion is defined as:

$$(\rho\beta)_{hnf} = \phi_{Al_2O_3} (\rho\beta)_{Al_2O_3} + \phi_{Cu} (\rho\beta)_{Cu} + (\rho\beta)_{bf} (1 - \phi) \tag{15}$$

where β_{bf} , $\beta_{Al_2O_3}$, and β_{Cu} are the coefficients of thermal expansion of water, alumina, and copper, respectively.

The thermal diffusivity (α_{hnf}) is determined as:

$$\alpha_{hnf} = \frac{k_{hnf}}{(\rho C_p)_{hnf}} \tag{16}$$

where the thermal conductivity k_{hnf} is determined from:

$$\frac{k_{hnf}}{k_{bf}} = \left(\frac{\phi_{Al_2O_3} k_{Al_2O_3} + \phi_{Cu} k_{Cu}}{\phi} + 2k_{bf} + 2(\phi_{Al_2O_3} k_{Al_2O_3} + \phi_{Cu} k_{Cu}) - 2\phi k_{bf} \right) \times \left(\frac{\phi_{Al_2O_3} k_{Al_2O_3} + \phi_{Cu} k_{Cu}}{\phi} + 2k_{bf} - 2(\phi_{Al_2O_3} k_{Al_2O_3} + \phi_{Cu} k_{Cu}) + 2\phi k_{bf} \right)^{-1} \tag{17}$$

The effective dynamic viscosity of the hybrid nanofluid is defined as:

$$\mu_{hnf} = \frac{\mu_{bf}}{(1 - \phi)^{2.5}} \tag{18}$$

where μ_{bf} is the dynamic viscosity of water. The thermophysical characteristics of the water, Cu and Al₂O₃ that are the constituents for the hybrid nanofluid are listed in Table 1.

3. Numerical Method and Validation

The dimensionless governing equations with the specified boundary conditions in Section 2 are solved by the Galerkin finite element method using the Multiphysics COMSOL software. In this method, the non-linear partial differential Eqs. (1-9) that define the mass and heat transport through the convection cell of Fig. 1 are integrated to obtain equivalent statements of conservation of mass, momentum, and energy in what is referred to in mathematics as the “weak” (integral) form. This integration procedure makes use of polynomials that provide the local variation of the state variables [51, 52]. For this purpose, P2-P1 Lagrange polynomials are used [53] that are applied to each finite-element in which the computational domain is discretized. The distribution of the state variables is continuous within each finite-element, as represented by the polynomials, but it is discontinuous across the boundaries between neighboring finite elements. This technique is referred to as the discontinuous Galerkin technique [54, 55] and it is the solution method implemented in COMSOL.

Table 2. Mesh Convergence Index with percentage error using Richardson's extrapolation at $S = 0.5$, $N = 1$, $Ra = 10^6$, $Da = 10^{-3}$, $\phi = 0.04$.

ζ	r	GCI21	GCI23	ϵ_1 (%)	ϵ_2 (%)	ϵ_3 (%)
Ψ_{min}	2	0.092	0.015	0.455	0.073	0.012
Nu_{hnf}	2	0.076	0.016	0.298	0.061	0.031
Nu_s	2	0.074	0.011	0.402	0.059	0.009



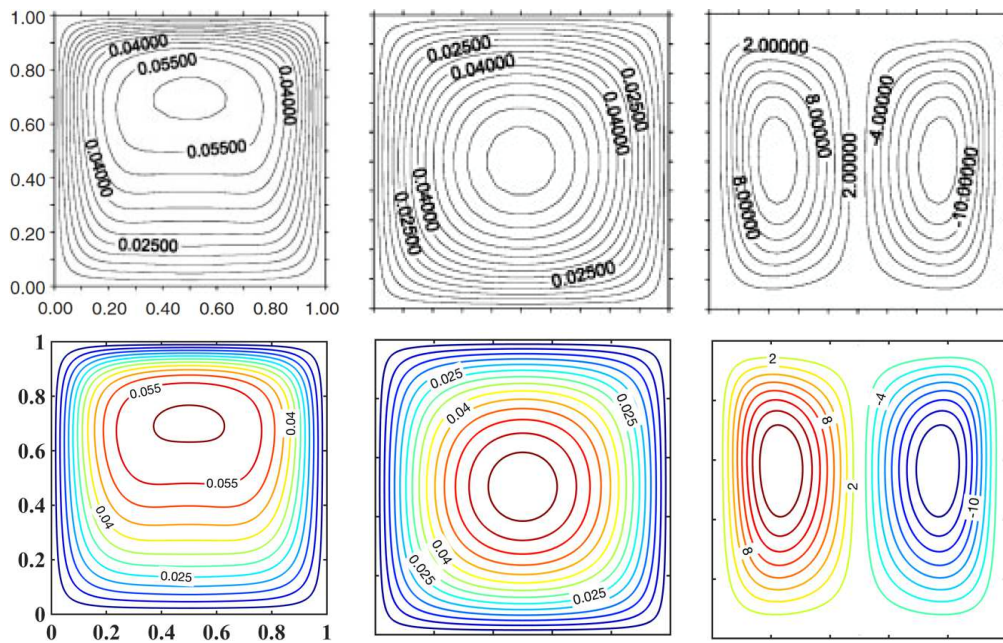


Fig. 2. Isotherms of the fluid and solid phases and streamlines (upper row), Baytas [58], and present study (lower row), at $Da = 10^{-2}$, $Ra = 10^7$, $\epsilon = 0.4$, $Pr = 0.7$, $Fo = 5.648$, $\gamma = 10^{-3}$ and $H = 500$.

The simulation provides steady-state flow predictions and the numerical method that iteratively improves a user-prescribed initial guess of the flow is the pseudo-time step iteration one. This is implemented by adding an artificial time derivative term to the left hand side of the conservation equations, which is used to evolved the flow over pseudo-time step iterations, until the flow state becomes substantially invariant between successive iterations [55]. The artificial time derivative term used in the X-momentum Eqs. (2) and (6) is:

$$\frac{U_{hnf} - nojac(U_{hnf})}{\Delta \tilde{t}} \tag{19}$$

where $\Delta \tilde{t}$ represents a pseudo time step and $[U_{hnf} - nojac(U_{hnf})]$ is a flow velocity change term determined in COMSOL. Similar artificial time derivative terms are used in the transport equations for V_{hnf} and for θ , which are obtained by replacing U_{hnf} with V_{hnf} and with θ in Eq. (19). In each finite-element, the pseudo-time step $\Delta \tilde{t}$ is selected so that the local CFL number CFL_{loc} does not exceed 1060. The pseudo-time step is related to CFL_{loc} as:

$$\Delta \tilde{t} = CFL_{loc} \frac{h}{\sqrt{U_{hnf}^2 + V_{hnf}^2}} \tag{20}$$

where $h = \max(\Delta X, \Delta Y)$ represents the finite-element size. At the start of the computation, $CFL_{loc} = 1.3$ provides numerical stability. Thereafter, CFL_{loc} is increased by 30% per iteration, up to the ninth iteration, where $CFL_{loc} = 10.6$. Between iterations 10 and 20, CFL_{loc} is kept constant at 10.6. Thereafter, between iterations 20 and 40, CFL_{loc} is progressively increased up to 106. After iteration number 40, it is progressively increased to 1060.

The Semi-Implicit Method for Pressure-Linked Equations (SIMPLE) is utilized to handle the pressure-velocity coupling. The residuals of the linearized equations are used to solve for the dependent variables by the Newton-Raphson method. The Newton-Raphson method is deemed to have converged to a steady solution at the $(m+1)^{th}$ iteration if:

$$\frac{\sum_{i=1}^I \sum_{j=1}^J |\chi_{i,j}^{m+1} - \chi_{i,j}^m|}{\sum_{i=1}^I \sum_{j=1}^J |\chi_{i,j}^{m+1}|} \leq 10^{-6} \tag{21}$$

where χ is any dimensionless scalar primitive variable (pressure, velocity components and temperature) within the computational domain. The subscripts i and j are, respectively, the i th and j th grid cell in the horizontal and vertical directions of the $I \times J$ structured computational domain. The simulations are performed on a computer with an Intel processor Core i7-8700M CPU with 3.20 GHz clock speed and 16 GB RAM. One simulation run typically converges within about four minutes of computer wall time.

In order to investigate the influence of the spatial discretization on the accuracy of the results, a grid convergence study is performed based on Richardson's extrapolation that is generalized by Roache [56]. In the current work, three grids are used to discretize the computational domain of Fig. 1 with a constant grid refinement ratio $r = 2$. These are a coarse grid of 70×70 cells (grid 1), a grid of intermediate spatial refinement of 140×140 cells (grid 2), and a fine grid of 280×280 cells (grid 3). The grid convergence index (GCI) examines how the dependent variables in the linearized governing equations approach their asymptotic values and therefore evaluates the appropriateness of the spatial resolution level. Two GCIs are calculated, according to [57], based on the average Nusselt number for the fluid phase (Nu_{hnf}), the average Nusselt number for the solid phase (Nu_s), and the streamfunction minimum (Ψ_{min}), for the representative case of $S = 0.5$, $N = 2$, $H = 10$, $\gamma = 10$, Darcy number of 10^{-3} , Rayleigh number of 10^6 , and a hybrid nanoparticles volume fraction of 4%. The predicted values of the streamfunction Ψ minimum for the three grids are -24.489, -24.369 and -24.381. The corresponding values of the average Nusselt number of the hybrid nanofluid and solid phases are 16.422, 16.461, 16.469 and 15.687, 15.741 and 15.749.



Table 3. Comparison of the average Nusselt number for $Da = 10^{-2}$, $\phi = 0.05$, $Ra = 10^7$, Hartman number = 0, and $D = B = 0.5$.

ϕ	Gorla et al. [32]	Present study	% Difference
0.02	0.062	0.063	1.59
0.04	0.057	0.059	3.39
0.06	0.053	0.055	3.64
0.08	0.048	0.049	2.04
0.1	0.044	0.046	4.35

Table 2 illustrates that the GCI calculated from the Ψ_{\min} predicted with the coarse grid and that with the intermediate grid is 0.092. This is larger than the GCI calculated from the Ψ_{\min} predicted with the intermediate grid and that with the fine grid, which is 0.015. Similar reductions in GCI are obtained for the CGI based on the average Nusselt numbers of the hybrid nanofluid phase and of the solid phase. This evidences a reduction in the grid dependence of the predicted results in which the intermediate and the fine grids are selected. The relative error shown Table 2 is calculated based on the difference between the predicted value ζ_i using the i th grid and Richardson's extrapolation ζ_R as $\varepsilon_i = \zeta_i / \zeta_R - 1$. Table 2 shows that for ε_i based on either Ψ_{\min} , Nu_{hnf} , Nu_s , the difference in the relative errors between the intermediate grid and the fine grid is below 0.1%, which identifies a satisfactory grid convergence, therefore the grid of intermediate spatial resolution is chosen for the current study.

The analytical representation of the enclosure heat and mass transfer and its numerical solution by the discontinuous Galerkin approach are validated by comparison with published numerical results in Nguyen et al. [10], Gorla et al. [32], Baytas [58] and with experiments from Beckermann et al. [59]. Baytas [58] studied the effect of local thermal non-equilibrium on the natural convection in a porous square enclosure with heat generation. Figure 2 reproduces the test case from Baytas [58] at $Da = 10^{-2}$, $Ra = 10^7$, $\varepsilon = 0.4$, $Pr = 0.7$, $Fo = 5.648$, $\gamma = 10^{-3}$ and $H = 500$. Steady predictions of the temperature in the fluid and in the porous medium are reported in individual isotherm plots. The steady flow induced by natural convection is shown by a plot of streamlines. The individual isotherm plots serve to expose the thermal non-equilibrium between the two phases, which is a specific validation feature for the present study. The upper row of Fig. 2 shows the results obtained from Baytas [58] and the lower row shows the results from the present study. The model in the present study is shown to predict with clarity the different temperature fields due to thermal non-equilibrium of this test case.

Gorla et al. [32] modelled an enclosure with walls at different temperatures, containing porous material and nanofluid, under different nanoparticle volume fraction conditions. Table 3 compares the average Nusselt number at the hot walls predicted by the current method with the equivalent ones from Gorla et al. [32] over the nanoparticles volume fraction range 0.02 to 0.1. Table 3 shows a good quantitative agreement with an average Nusselt number discrepancy of less than five percent.

To further increase the confidence in the results obtained from the current numerical method, Fig. 3 shows comparisons with previous experimental results of Beckermann et al. [59] and with numerical results of Nguyen et al. [10]. These concern an enclosure containing layers of porous material, with its opposing side walls set at different temperatures. More details on the geometry and material properties is available in Beckermann et al. [59]. Figure 3 shows the non-dimensional temperature along the normalized x-coordinate at $Y = 0.874$. The current numerical results are shown to be in good agreement with the ones reported by Beckermann et al. [59] and by Nguyen et al. [10].

These comparisons give trust in using the current CFD method for a comparative analysis including the effect of various effective parameters introduced in the next section.

4. Results and Discussion

This section reports the results of the numerical simulations. Different configurations are compared using composite figures with the common layout of (a) streamlines on the left, (b) isotherms of the hybrid nanofluid at the center, and (c) isotherms of the solid phase on the right. The enclosure overall thermal performance is expressed in terms of the average Nusselt number over the heated wall. Two Nusselt numbers are provided, based on the temperature gradient of the hybrid nanofluid and of the solid matrix across the porous layer.

The enclosure heat and mass transfer performance is examined in Sections 4.1 and 4.2 for different values of the Darcy number ($10^{-5} \leq Da \leq 10^{-2}$), porous medium height ($0 \leq H_p \leq 1$), number of undulations ($1 \leq N \leq 5$), and modified conductivity ratio ($0.1 \leq \gamma \leq 1000$). The nanoparticle volume fraction is varied between 0 and 0.04, with $\phi_{Cu} = \phi_{Al_2O_3}$. The Rayleigh number, the interphase convection heat transfer coefficient, and the porosity of the porous medium are kept constant at $Ra = 106$, $A = 0.1$ L, $H = 10$, and $\varepsilon = 0.398$, respectively. The effect of varying Ra , H , and ε are explored in [60] and the expectation is that the current enclosure will exhibit a similar behavior. This study therefore explores the effects of other, less explored, parameters.

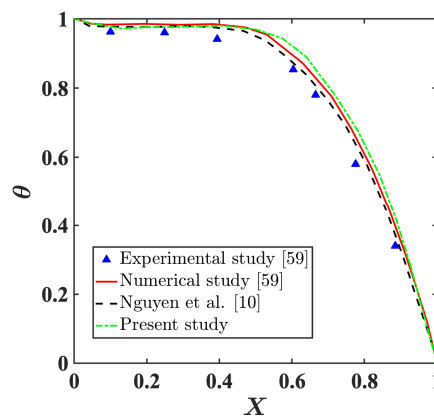


Fig. 3. Non-dimensional temperature distribution at constant height $Y = 0.874$ along the length of a rectangular enclosure layered by porous material, with the opposing side walls kept at different temperatures. Current model validation against numerical and experimental results of Beckermann et al. [59] and numerical results of Nguyen et al. [10].



4.1 Streamlines and isotherms

Figure 4 shows the effect of the dimensionless permeability (Darcy number) and of the nanoparticle volume fraction ϕ on the streamfunction (left column), on the hybrid nanofluid phase temperature distribution (central column), and on the solid phase temperature distribution (right column), at $H_p = 0.5$, $N = 2$, and $\gamma = 10$. For each Darcy number, the flow motion and the distributions in temperature for the hybrid nanofluid (dashed lines) are compared versus the results obtained by using pure water (solid lines). Figure 4 illustrates in the left column the ability of the fluid to permeate the porous layer, based on the value of the Darcy number. In this column, the streamlines show that two main recirculation cells form inside the enclosure, generated by the buoyancy of the hybrid nanofluid heated at the bottom wavy wall and cooled at the left and right straight vertical walls. Heating generates a single upwell towards the center of the enclosure and two downwards fluid return paths along the left and right vertical walls, respectively. This produces the clockwise recirculation cell localized in the left half of the enclosure and the anticlockwise recirculation cell in the right half of the enclosure. These cells penetrate by different extents into the porous layer. At $Da = 10^{-5}$, the left column of Fig. 4 shows by the streamlines that the hybrid nanofluid layer includes most of the recirculation while the porous layer shows a more modest motion through it. Increasing the Darcy number increases the porous layer penetration of the hybrid nanofluid flow, as indicated by higher streamfunction magnitudes $|\Psi|$ through it. The large motion through the porous layer displaces the center of the two cells towards the heated bottom wall. Qualitatively the same trend is obtained with pure water and with hybrid nanofluid, as shown by the dashed lines tracking well the continuous lines in the left column of Fig. 4. The addition of 4 % by volume of nanoparticles to the pure water leads to a decrease in the value of $|\Psi|$ over the considered range of Da . This is due to the higher viscous dissipation in the hybrid nanofluid, due to its higher dynamic viscosity compared to pure water, as stated in Eq. (18).

The convection cells are asymmetric and their relative strength varies with the Darcy number. At $Da \leq 10^{-3}$, $|\Psi_{\min}| < |\Psi_{\max}|$ and the right clockwise cell has a stronger flow. The right cell develops above the convex section of the bottom wall. This convexity is shown to push the flow away from the heated wall, as shown by the recirculation cell center lying above that of the left cell. The saddle plane that separates the two recirculation cells is oblique and this allows the right cell to fill a greater area of the hybrid nanofluid layer than the left cell. The same feature confines the right cell to a narrower area of the porous layer than the left cell. The right cell flow recirculates over a comparatively larger area of hybrid nanofluid layer, where the resistance to flow is lower than in the porous layer. This produces the stronger clockwise flow. At $Da = 10^{-2}$, it is the left cell to exhibit the stronger flow as indicated by $|\Psi_{\min}| > |\Psi_{\max}|$. At this higher Darcy number, Fig. 4 shows that the left recirculation cell sits mostly inside the bottom porous layer and wets most of the bottom heated wall. The concavity of the heated bottom wall matches the sign of the curvature of the (concave) streamlines lapping it. The combination of buoyancy forces, due to heating from the bottom wall, and of the natural curvature alignment between the streamlines and the concave wall appear to support a stronger recirculation and therefore appear to overcome the flow resistance penalty from the left cell residing mainly in the porous layer.

At the highest value of $Da = 10^{-2}$, the isotherms in Fig. 4 (center and right) are densely packed above the heated wavy wall and run from each bottom corner towards the saddle point that separates the two recirculation cells on this wavy wall. The isotherms of hybrid nanofluid contour around the saddle point, highlighting this point as a potential temperature hotspot. Specifically, the reduction in the wall-normal temperature gradient reduces the rate of cooling by convection. In the absence of any porous medium, this would be a cause for concern in a practical engineering application, such as in the even cooling of a microprocessor chip. The presence of the porous layer is shown in Fig. 4 (right) to produce a wall-normal temperature gradient in the porous medium at the saddle point. This alleviates the risk of hot spot formation, due to the lower convection by the hybrid nanofluid, by providing heat conduction through the porous matrix.

Along the left and right walls, the isotherms in Fig. 4 (center and right) are vertically aligned with the wall, particularly at the higher values of Da , for the pure fluid and the hybrid nanofluid. It can be observed from Fig. 4 that augmenting the permeability of the porous medium causes denser isothermal lines packed along the bottom hot wavy wall, these isotherms following the wall geometry. The packing in isotherms explains the increment in temperature gradients close to the wall which is due to the high conductivity ratio improving the convective heat transfer performance. The isotherms emanate from the bottom right and left corners, where the constant temperature hot wavy bottom wall encounters the constant temperature cold vertical walls. This is where the temperature gradient is highest in the enclosure.

The pattern of isotherms of the working fluid in Fig. 4 (center) is consistent between the simulations that use hybrid nanofluid and the ones using pure water, as shown by the dashed lines following a path similar to that of the continuous lines. Some differences are noticeable in the hybrid nanofluid layer at the top of the enclosure, where the thermal gradients are weakest. The same observation can be made about the temperature distribution of the solid matrix in Fig. 4 (right), which is rather similar whether the enclosure is saturated by water or by hybrid nanofluid. This result reinforces the conclusion in [61] about the addition of nanoparticles affecting the heat transfer performance but not changing the fundamental convection heat transport path. Ali et al. [61] concluded that this allows the design and testing of microchannel heat sinks using pure water, then to fine-tune the thermal performance by adding nanoparticles.

Figure 4 (center) and Fig. 4 (right) compare and contrast the temperature fields of the fluid and of the solid matrix in the porous layer. At the lowest value of $Da = 10^{-5}$, the isotherms of the solid and fluid are rather similar, with only minor differences approaching the interface between the hybrid nanofluid region and the porous region. The low permeability in this condition creates significant resistance to flow, so that the fluid in the pores has sufficient time to develop a local thermal equilibrium with the solid matrix around it. Over the range $10^{-4} \leq Da \leq 10^{-2}$ differences between the two temperature fields emerge, at first along the saddle plane that separates the two convection cells, at $Da = 10^{-4}$, then also alongside the vertical walls, at $Da = 10^{-2}$. The simulation at $Da = 10^{-2}$ exposes three important points in Fig. 4 (center), which are just above the bottom corners of the enclosure and the saddle point on the bottom wavy wall. All these three locations exhibit Ω -shaped isotherms of working fluid temperature around these points. They identify these points as locations of reduced wall-normal temperature gradient of the working fluid and therefore as potential hot and cold spots. Such features are unwelcome, as they typically lead to early degradation of the material properties in heat exchangers. Figure 4 (right) shows no such Ω -shaped isotherms in the solid matrix temperature distribution. It evidences the usefulness of the solid matrix in palliating the hot-spot effect, by compensating lack of localized heat convection by heat conduction. Hot and cold spots do not form on the enclosure bottom and side walls, since these walls are modelled as constant temperature surfaces. Still, the simulation has highlighted processes and locations where hot and cold spots are likely to occur in applications where the heat flux, rather than the temperature, is prescribed over these surfaces.

Resolving the local thermal non-equilibrium in the model is shown to be of vital importance in this application. Without this level of modelling, there would have been no means for differentiating the roles the flow and the solids have in determining the local heat transfer rates along the walls. The process of hot spot and cold spot generation would have been masked by the single temperature field used in local thermal equilibrium simulations. It is clear that the LTNE approach adopted by the authors has provided new insight into this class of flows.



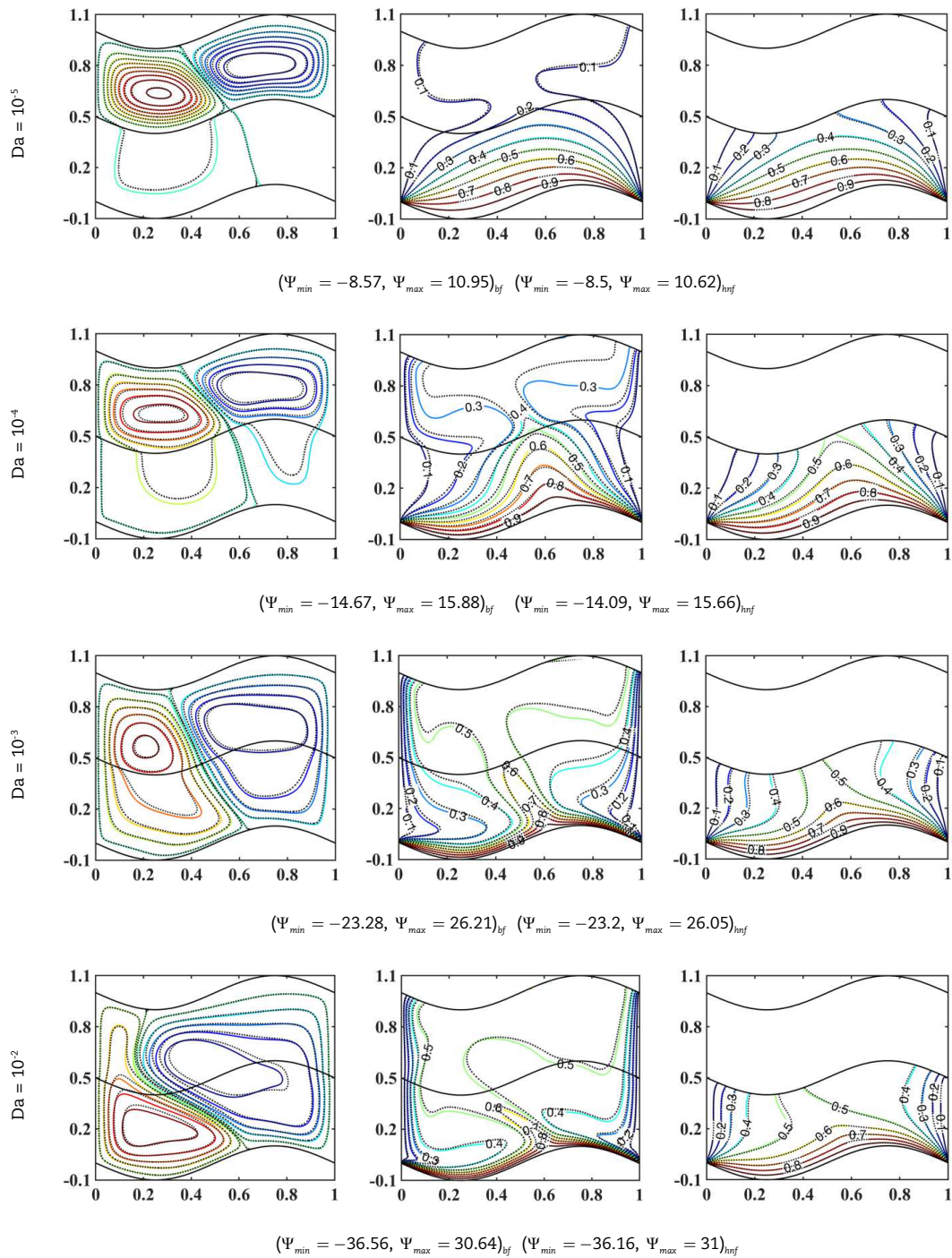


Fig. 4. Streamlines (left column), isotherms of the hybrid nanofluid phase (central column), and isotherms of the solid phase (right column), for different Darcy numbers, at $\gamma = 10$, $N = 2$, and $H_p = 0.5$, $\phi = 0$ (solid lines) and $\phi = 0.04$ (dashed lines).

Figure 5 shows the effect of varying the height of the porous layer H_p on the natural convection flow and temperature distributions, at $Da = 10^{-3}$, $N = 2$, and $\phi = 0$ and 0.04 . The streamlines on the left column in Fig. 5 show qualitatively the same pattern of two convection cells as in Fig. 4, with both Cu-Al₂O₃ hybrid nanofluid (dashed black lines) and pure water (solid colored lines). The shape and center of these two convection cells vary depending on the porous layer height. Without a porous layer $H_p = 0$, the topmost plot on the left column of Fig. 5 shows that the anti-clockwise left convection cell has a smaller extent than with a porous layer and that it is confined towards the bottom left corner. The absence of the porous layer enables the cell center to sit closer to this corner, as there is no resistance to flow promoting the circulation to sit preferentially away from the bottom wall. At $H_p = 0.3$, the two circulation cells cover areas of similar size in the enclosure and the saddle surface that parts the two circulation cells is reasonably planar. The clockwise right convection cell occupies most of the fluid layer, it has an elliptical shape, and its center is located almost in the middle of the fluid layer. The clockwise left convection cell is more circular in shape and its center is located closer to the interface between the porous and fluid layers. Figure 5 shows that increasing the porous layer height reduces the $|\Psi|$ maxima with both pure water and hybrid nanofluid. This reduction in circulation cell strength, which is highest at $H_p = 1$, is due to the hydrodynamic resistance of the porous medium.



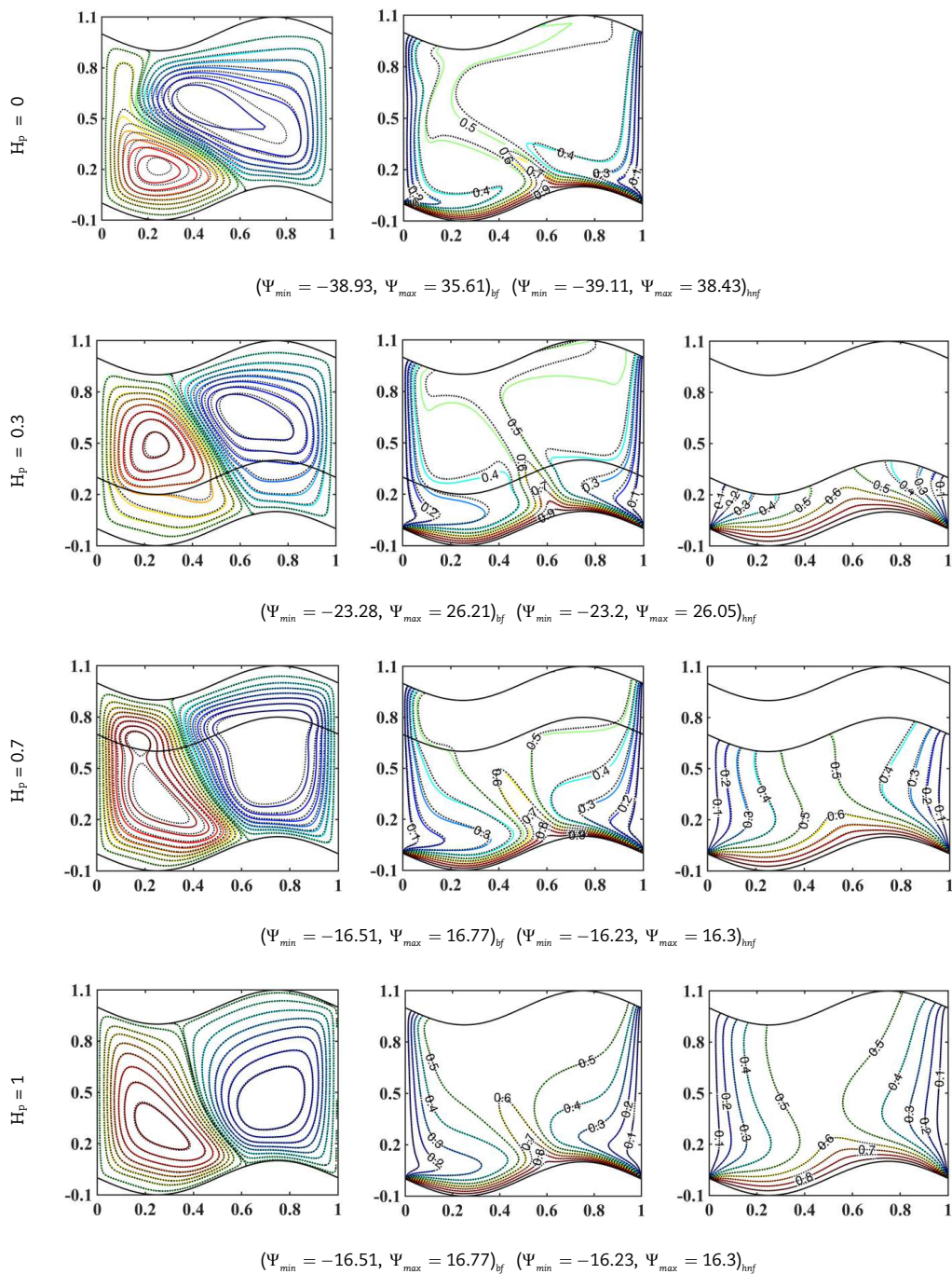


Fig. 5. Contours of streamlines (left column), isotherms of the hybrid nanofluid phase (central column), and isotherms of the solid phase (right column), for different porous layer heights, at $\gamma = 10$, $N = 2$, and $Da = 10^3$, $\phi = 0$ (solid lines) and $\phi = 0.04$ (dashed lines).

The reduction in circulation affects the isotherms of the fluid and of the porous matrix. Specifically, the central column in Fig. 5 shows that increasing the porous layer height H_p progressively reduces the packing, or clustering, of the isotherms near the walls. For instance, isotherm $\theta = 0.2$ that runs close to the left cold wall at $H_p = 0$ runs progressively more through the enclosure interior at increasing H_p values. This reduction in the wall-normal temperature gradient indicates a reduced convective heat transfer rate from the working fluid through the constant temperature walls. In the enclosure, the isotherm $\theta = 0.5$ outlines a central region where the temperature of the fluid $\theta > 0.5$ is closer to that of the bottom wall and two regions either side of it, where the temperature of the fluid $\theta < 0.5$. At $H_p = 0$ and $H_p = 0.3$, the central region where $\theta > 0.5$ remains relatively narrow in X over the range $0.2 \leq Y \leq 0.8$. It widens substantially at $H_p = 0.7$ and $H_p = 1$. Whilst coolant fluid degradation is typically linked to localized over-heating events at hot spots, its long-term degradation can be affected by its average operating temperature. These predictions indicate that the thicker porous layers cause the coolant to remain at $\theta > 0.5$ across larger extents of the enclosure, which is less preferable from a fluid degradation prospective than a lower average working temperature, at the same overall heat transfer rate. The isotherms of pure water and of hybrid nanofluid follow broadly similar paths at $H_p = 0$ and their alignment in path increases with increasing porous layer thickness until they essentially overlap at $H_p = 1$. At $H_p = 0$ and $H_p = 0.3$, the wall-normal temperature gradient for the fluid phase is increased by adding the hybrid nanoparticles to the pure fluid. At $H_p = 1$ the two working fluids display essentially the same temperature distribution, however, they retain a difference in heat convection and conduction due to their different thermal conductivity and constant pressure specific heat capacity.



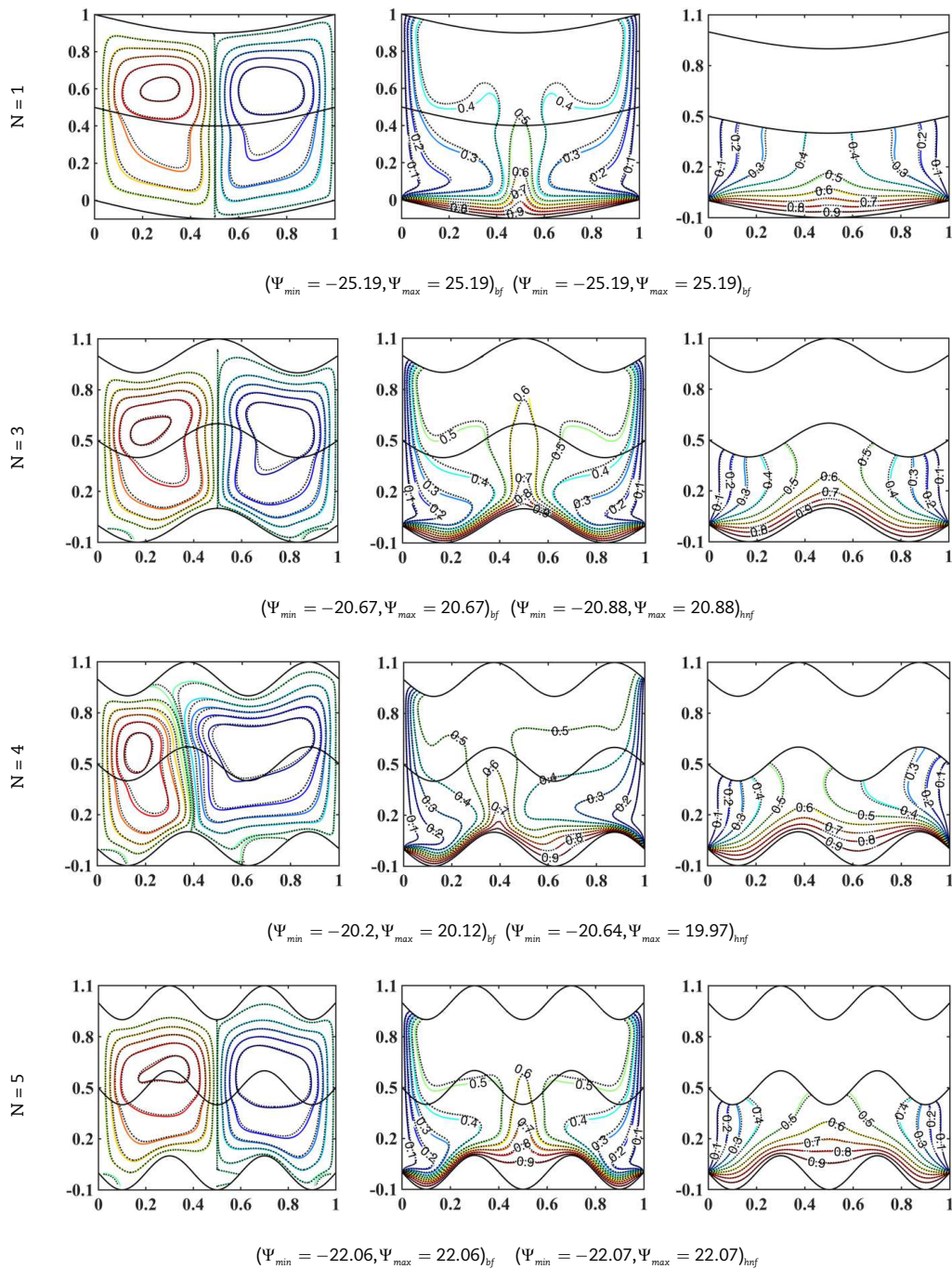


Fig. 6. Streamlines (left column), isotherms of the hybrid nanofluid phase (central column), and isotherms of the solid phase (right column), for different wavy wall wavenumbers N at $\gamma = 10$, $H_p = 0.5$, and $Da = 10^{-3}$, $\phi = 0$ (solid lines) and $\phi = 0.04$ (dashed lines).

The non-dimensional temperature distribution of the solid phase, shown by the right column of Fig. 5, follows broadly the same trend as that in Fig. 4. The isotherms are less packed compared to the corresponding working fluid isotherms in the central column of Fig. 5. The porous matrix is shown to retain its important role of providing wall-normal temperature gradients in the areas where cold and hot spot formation mechanism are present, as discussed in Fig. 4, which are likewise present at all H_p values in Fig. 5 (central column).

Figure 6 shows that the number of undulations N has a significant effect on the flow and temperature distribution inside the enclosure, at $Da = 10^{-3}$, $H_p = 0.5$, $\gamma = 10$, with both hybrid nanofluid at $\phi = 0.04$ (dashed black lines) and with pure water, at $\phi = 0$ (solid color lines). If N is odd, then two symmetric convection cells of equal strength form either side of the $X = 0.5$ plane, which is also a $\Psi = 0$ line of the streamline map. If N is even, Fig. 4 and Fig. 6 show an asymmetric convection cell pattern, with an oblique and curved $\Psi = 0$ line separating the two convection cells. The two cells occupy unequal areas in the enclosure, the right clockwise convection cell being larger. The strength of the two convection cells is uneven, as shown by the difference in $|\Psi|$ maxima. This fundamental behavior is unaffected by the concentration of nanoparticles, as shown by the solid lines and the dashed lines both showing this trend. The highest recirculation strength is obtained at $N = 1$, whereas increasing the number of undulations is detrimental to the circulation strength of the hybrid nanofluid that runs through the porous layer. At $N = 1$ and 2, the streamlines follow the undulations of the top and bottom walls, from the side walls up to the upwell point, where the two convection cells meet. At $N \geq 3$, secondary recirculation cells of separated flow form in the troughs of the heated wavy wall. These areas of near-stagnant flow are likely to be detrimental to the thermal transport performance of the enclosure.



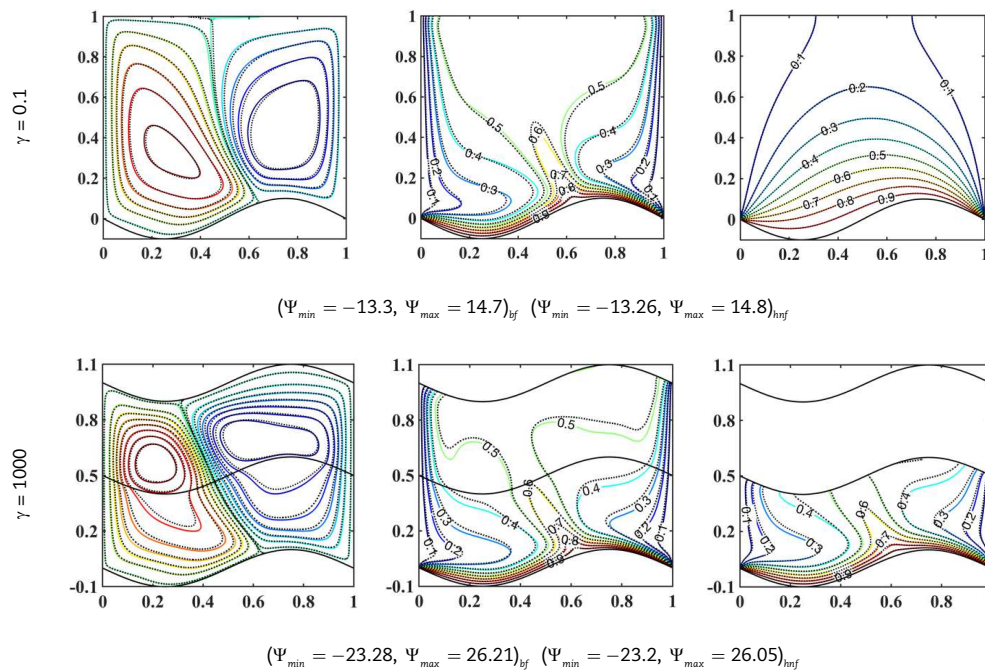


Fig. 7. Streamlines (left column), isotherms of the hybrid nanofluid phase (central column), and isotherms of the solid phase (right column), for different modified conductivity ratios, at $\gamma = 10$, $N = 2$, $H_p = 0.5$ and $Da = 10^3$, $\phi = 0$ (solid lines) and $\phi = 0.04$ (dashed lines).

Some evidence of this detrimental effect is provided by the temperature distribution of the working fluid in the central column of Fig. 6. Along the peaks, or crests, of the undulations on the bottom wall, where the streamlines follow the contour of the wall, the isotherms are tightly packed, indicating a good wall-normal temperature gradient and good conditions for heat transport by convection. Conversely, in the troughs where localized flow separations are present, the isotherms are less packed, indicating a weaker temperature gradient normal to the heated surface. At $N = 5$, the $\theta = 0.9$ isoline at $X = 0.5$ runs almost horizontal between the wall crests either side of $X = 0.5$. This indicates a rather low temperature gradient in the central trough. This identifies the central trough as a region of weak heat exchange between the wall and the enclosure. For the fluid phase, the higher packing of the isotherms towards the wall indicates that the wall-normal temperature gradient increases by adding nanoparticles to the pure fluid at $N = 1, 3$, and 5 while for $N = 4$ the dashed line isotherms overlap the solid line isotherms, indicating essentially the same temperature gradients with and without nanoparticles.

The temperature distribution of the solid matrix reported on the right column of Fig. 6 gives a valuable insight on how the thermal conductivity of the porous matrix is able to assist the convection heat transfer from the working fluid. As in Fig. 4 and in Fig. 6, wall-normal thermal gradients form at either bottom corner, where the Ω shaped isotherms of the working fluid indicate an unwanted cold spot mechanism. A similar heat conduction effect is provided at the confluence of the two main recirculation cells above the heated bottom wall. However, in the troughs of the bottom heated wall, where the flow is locally separated, the isotherms of the porous matrix remain rather distant from one another and the support from conduction through the matrix to the heat transfer away from the heated wall is rather weak. This indicates that an alternative palliative strategy is required in these areas, which aim at preventing the formation of these secondary recirculation regions in the first place.

Figure 7 shows the effect of changing the modified conductivity ratio, from $\gamma = 0.1$ to $\gamma = 1000$ on the streamlines, on the isotherms of the hybrid nanofluid, and on the isotherms of the porous matrix, at $Da = 10^3$, $N = 2$, and $H_p = 0.5$. with both pure water, $\phi = 0$ and hybrid nanofluid, at $\phi = 0.04$. By comparing the streamlines in the left column of Fig. 7 with the ones at $Da = 10^3$ and $\gamma = 10$ in Fig. 4 (left column), no significant change in the flow motion is obtained by varying γ over four orders of magnitude. There is a slight reduction in the strength of the circulation as γ is changed from 0.1 to 10, as shown by the $|\Psi|$ maxima, but no further reduction is predicted between $\gamma = 10$ and $\gamma = 1000$. The isotherms of the working fluid shown in the central column of Fig. 7 and Fig. 4 at $Da = 10^3$ are likewise substantially invariant on γ , with both pure water and with the hybrid nanofluid.

More significant is the effect of changing the modified thermal conductivity ratio on the temperature distribution of the porous matrix, as shown by the right column in Fig. 7 and at $Da = 10^3$ in Fig. 4. The isotherms of the porous matrix fan across the porous matrix from the corners of the enclosure bottom. At $\gamma = 0.1$, the resulting two isotherm fans feature isotherm lines with a regular angular spacing, a pattern that characterizes classical solutions of the Laplace equation. This indicates that the temperature distribution through the porous matrix is mainly determined by the ability of heat to move through it by conduction, rather than by the temperature of the fluid that saturates it. As γ increases, the isotherms of the porous matrix assume progressively the same pattern as the ones of the working fluid in the central column of Fig. 4 and of Fig. 7. At these conditions, the porous matrix acts progressively more like a thermal insulator. The poor thermal conductivity through it is such that the porous matrix assumes the temperature of the fluid that saturates it. The lack of conduction through the porous matrix is detrimental to the performance of the enclosure as a heat transfer device, as the matrix just produces unwanted flow resistance to flow in the convection cells at these conditions. Just above the two bottom corners as well as at $X = 0.5$ on the bottom wall, the porous matrix isotherms at $\gamma = 1000$ retain locally the Ω -shapes that are mechanisms for the formation of two cold spots and one hot spot. The low thermal conductivity through the porous matrix is unable to transfer heat away from these locations and to palliate the lack of convection in these regions of near-stagnant flow. At $\gamma = 1000$, the working fluid and the porous matrix are almost in thermal equilibrium, as they display very similar temperature distributions. At this condition, the local thermal non-equilibrium model used in the simulation becomes unnecessary. These observations apply to both the hybrid nanofluid and to the pure water simulations.



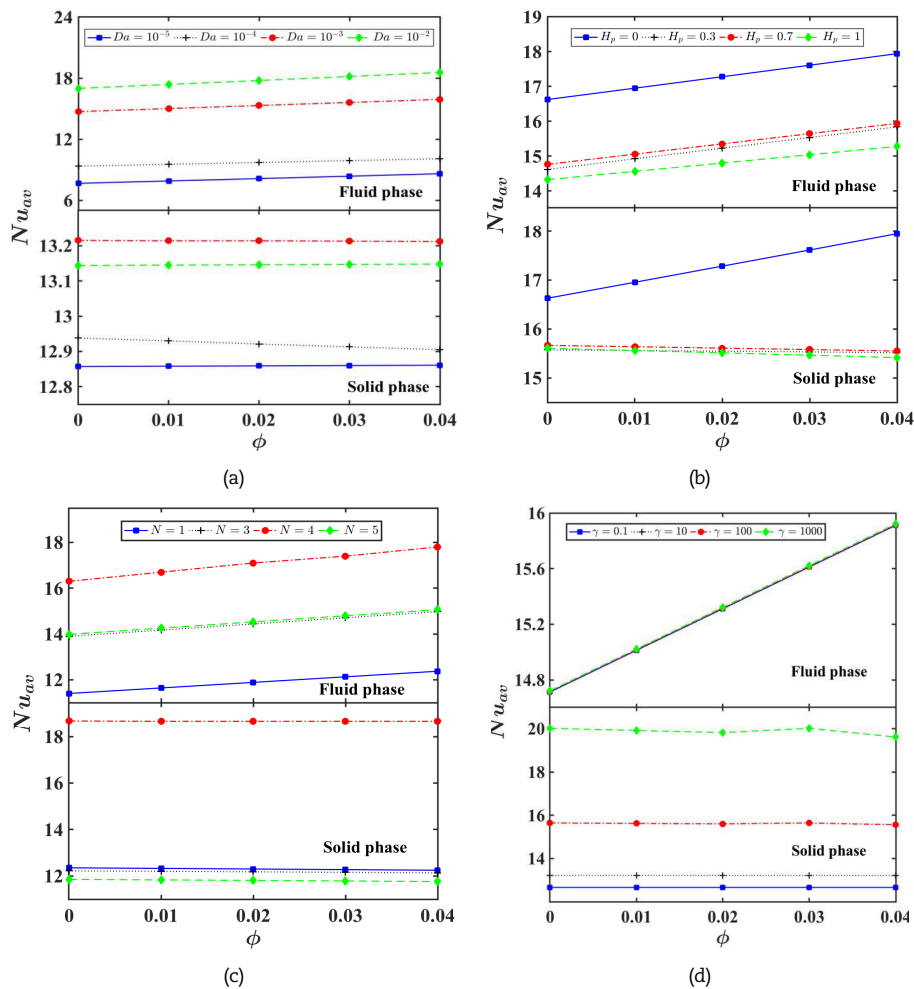


Fig. 8. Variation of the average Nusselt number of the fluid phase (the upper part) and of the solid phase (the lower part), with ϕ for different (a) Da , (b) H_p , (c) N , and (d) γ .

4.2 Average Nusselt number

It is illustrated in Section 4.1 that resolving the Local Thermal Non-Equilibrium (LTNE) in the enclosure produces significant differences between the temperature distributions in the porous matrix and in the working fluid at a number of working conditions. This section explores the relationship between the average Nusselt number (Nu_{av}) on the bottom heated wavy wall of the enclosure and the nanoparticle volume fraction (ϕ) for different values of Darcy number, in Fig. 8(a), of porous layer height, in Fig. 8(b), of number of undulations, in Fig. 8(c), and of modified thermal conductivity ratio, in Fig. 8(d). The Nusselt number based on the working fluid temperature gradient at $\gamma = 10$, $N = 2$, and $H_p = 0.5$ in Fig. 8(a) increases with increasing Da and ϕ . Changing Da has the greatest effect on Nu_{av} among the range of independent variables modelled in this study. The increase in porosity was shown in Fig. 4 (left column) to increase the strength of the convection cells and therefore the convection heat transfer in the enclosure. As discussed in Kadhim et al. [39] the higher thermal conductivity of the nanoparticles aids the convection heat transfer process by absorbing more easily heat within them, by conduction through their body, and transporting this heat from the hot wavy wall to the cold vertical walls, by nanoparticle motion, compared to pure water. This effect is present at all Darcy numbers in Fig. 8(a), as indicated by the monotonic increase in Nusselt number with nanoparticle concentration ϕ . The Nusselt number based on the temperature of the porous matrix is less sensitive to Da and ϕ , as shown in the bottom half of Fig. 8(a), where changes in Nusselt number are one order of magnitude smaller than the ones in the top half of Fig. 8(a). At $Da = 10^{-4}$, the addition of nanoparticles weakens the convection due to increased frictional losses, therefore in the porous medium an increment in nanoparticle concentration reduces the average Nusselt number. This trend is also present in previous studies [30, 62] of heat transport through porous media using non-equilibrium models. The increase in Da enhances the heat transfer rate, in agreement with the previous studies [63, 64].

The top part of Fig. 8(b) shows how the Nusselt number based on the working fluid temperature changes with the porous layer height and with the nanoparticle volume concentration, at $\gamma = 10$, $N = 2$, and $Da = 10^{-3}$. Increasing the porous layer height reduces this Nusselt number, mainly due to the reduction in the convection cell strength documented in the left column of Fig. 5, due to the greater flow resistance through the porous material. This reduction is non-monotonic, as Nu_{av} at $H_p = 0.7$ is higher than that at $H_p = 0.3$. At $H_p = 0.3$, the central column of Fig. 5 displayed a larger area of enclosure at $\theta \geq 0.5$ than at $H_p = 0$ and at $H_p = 0.3$. It is thought that the greater availability of relatively colder working fluid near the heated wavy wall at higher H_p values enables the onset of a larger wall-normal temperature gradient and this provides an explanation for this non-monotonic Nu_{av} change. The Nusselt number in the top part of Fig. 8(b) monotonically increases with nanoparticle concentration, as in the top part of Fig. 8(a), due to the same physical process related to the greater thermal conductivity of the nanoparticles compared to pure water explained in the context of Fig. 8(a).

The bottom part of Fig. 8(b) shows that the average Nusselt number based on the temperature of the porous matrix is relatively insensitive to both the porous matrix thickness and to the nanoparticle concentration. A change in these variables over the ranges $0 \leq H_p \leq 1$, and $0 \leq \phi \leq 0.04$, causes changes in this Nusselt number average over the heated wavy wall that are one order



of magnitude lower than in the Nusselt number average based on the working fluid temperature, shown in the top part of Fig. 8(b). Whilst these changes are comparatively small, it is of interest to note that the bottom part of both Fig. 8(a) and Fig. 8(b) display a monotonic reduction in Nu_{av} with increasing ϕ . This trend persists for different circulation strengths, in Fig. 8(a), and porous layer thicknesses, in Fig. 8(b), therefore, it is more likely to be related to a property-dependent effect rather than a geometry or flow-dependent effect. One possible explanation is obtained by considering the change in temperature the working fluid has as it absorbs heat near the wavy heated wall. The heat absorbed per unit volume is $\rho C_p \Delta T$. At $\phi = 0$, from equation (16) and Table 1, $(\rho C_p)_{hnf} = 4.17 \text{ MJ m}^{-3}\text{K}^{-1}$ and at $\phi = 0.04$, $(\rho C_p)_{hnf} = 4.13 \text{ MJ m}^{-3}\text{K}^{-1}$. Therefore, the hybrid nanofluid undergoes a 1% higher temperature rise than the base fluid, for the same amount of heat absorbed per unit volume. The porous matrix in contact with the heated wavy wall is exposed to the wavy wall temperature at the wall and to the temperature of the working fluid away from the wall. With the hybrid nanofluid temperature rise being 1% higher than that of pure water, for the same amount of heat absorbed per unit volume, the wall-normal temperature gradient experienced by the porous matrix saturated by hybrid nanofluid is likely to be reduced, leading to a slight reduction in the average Nusselt number, based on the porous matrix temperature.

Figure 8(c) illustrates the effect of changing the number of undulations of the wavy walls on the average Nusselt number along the heated wavy wall, for different values of nanoparticle volume fraction ϕ at $\gamma = 10$, $Da = 10^{-3}$, and $H_p = 0.5$. The average Nusselt number based on the working fluid temperature, shown in the top part of Fig. 8(c), monotonically increases with nanoparticle concentration, as in Fig. 8(a) and in Fig. 8(b). Over the range $0 \leq \phi \leq 0.04$, the average Nusselt number is the highest with the number of undulations $N = 4$, irrespective of whether the Nusselt number is evaluated based on the working fluid or on the porous matrix temperatures. The Nusselt number based on the working fluid temperature gradient is lowest at $N = 1$ and the one based on the porous matrix temperature gradient is lowest at $N = 5$. This is consistent with the changes in the packing density of the isotherms in the central and right columns of Fig. 6 discussed in Section 4.1. The average Nusselt number based on the porous matrix temperature gradient, shown in the bottom half of Fig. 8(c) is substantially insensitive to the change of the nanoparticle volume fraction at constant N , consistently with the bottom half of Fig. 8(a) and of Fig. 8(b).

Figure 8(d) shows the variations of the average Nusselt number with ϕ for various values of modified thermal conductivity ratios γ at $Da = 10^{-3}$, $N = 2$ and $H_p = 0.5$. The Nusselt number based on the nanofluid temperature gradient, shown in the top part of Fig. 8(d), is essentially insensitive to changes in the modified thermal conductivity ratio and increases monotonically with ϕ with a slope and over a range similar to the ones in Fig. 8(b). The Nusselt number based on the porous matrix temperature displays the opposite trend in the bottom part of Fig. 8(d), namely it is substantially insensitive to ϕ and it is mostly affected by changes in γ . At $\phi = 3\%$, the Nusselt number based on the porous matrix temperature gradient is marginally higher than that at other nanoparticle volume fractions, over the range $0 \leq \phi \leq 4\%$. The increase in Nusselt number based on the porous matrix temperature gradient was somewhat unexpected, since the reduced thermal conductivity of the porous matrix at increasing γ values, according to the definition of γ in section 2.2, would lead to a loss in heat transfer by conduction through the porous matrix. In Fig. 7 (right column), the porous matrix isotherms were observed to pack more tightly against the heated wall at increasing γ , providing a stronger wall-normal temperature gradient that may offset the reduced thermal conductivity of the porous matrix. Still, this increase in Nusselt number based on the porous matrix temperature is one aspect that warrants further investigation.

5. Conclusions

By applying a Galerkin finite element approach, this study was able to expose important local thermal non-equilibrium effects in the steady natural convection inside a two-dimensional enclosure with horizontally corrugated walls containing a bottom porous layer filled with Cu-Al₂O₃/water hybrid nanofluid. The flow and heat transfer inside this cavity were analysed using streamlines, isotherms of the hybrid nanofluid and of the porous matrix, and the average Nusselt number, over five dimensionless parameters (Da , H_p , N , ϕ , γ). The key findings of this analysis are:

- The effects of the local thermal non-equilibrium are substantial for high values of Darcy number and low values of the modified conductivity ratio.
- Altering the Darcy number produces the greatest change in the average Nusselt number over the heated wall and it is therefore the most effective variable among (Da , H_p , N , ϕ , γ) for adjusting the overall heat transfer rate, owing to its controlling effect on the circulation strength of the natural convection cells.
- The local thermal non-equilibrium model exposed important hot and cold spot formation mechanisms, not previously reported for this type of enclosure, and a useful mitigation mechanism for them by heat conduction through the porous matrix. Whilst this makes the porous layer useful to have, increasing in the porous layer height decreases the average Nusselt number.
 - The number of undulations N of the corrugated walls affects the circulation strength and the shape of the vortices in the entire enclosure, which are symmetric about $X = 0.5$ for N odd. Asymmetric convection cells provide a higher average Nusselt number.
 - Compared to the pure water, the addition of Cu-Al₂O₃ nanoparticles affects the circulation strength and increases the temperature gradients in the working fluid, which in turn enhances the heat transfer rate.
- The non-equilibrium model exposed a previously unreported reducing effect of the hybrid nanoparticle concentration on the porous matrix temperature gradient and hence on its average Nusselt number. Whilst small, this effect is of fundamental interest to conjugate heat transfer modelling.
- The average Nusselt number based on the porous matrix temperature gradient increases with increasing γ , while the one based on the working fluid temperature gradient is substantially unaffected by γ .

Author Contributions

H.T. Kadhim planned and initiated the project. Z.M. Al Dulaimi formulated and developed the mathematical modeling. A. Rona examined the validation of the results. This paper was written with the contribution of all authors. All authors discussed and analyzed the findings, reviewed, edited and approved the final version of the manuscript.

Acknowledgments

The authors acknowledge the University of Leicester for funding support of this study. Graphical rendering software was originally bought on EPSRC GR/N23745/01. Research Support Engineer assistance was received, established under HPC Midlands +, funded by EPSRC EP/T022108/1. Flow modelling strategies were supported by the partnership established under MR/T017988/1.



Conflict of Interest

The authors declared no potential conflicts of interest concerning the research, authorship, and publication of this article.

Funding

The authors received no financial support for the research, authorship, and publication of this article.

Data Availability Statements

The datasets generated and/or analyzed during the current study are available from the corresponding author on reasonable request.

Nomenclature

a	Amplitude [m]	Pr	Prandtl number
A	Dimensionless amplitude	Ra	Rayleigh number
C_p	Specific heat capacity [$\text{J kg}^{-1} \text{K}^{-1}$]	T	Temperature [K]
Da	Darcy number	U, V	Non-dimensional components of velocity in X and Y directions
g	Acceleration due to gravity [m s^{-2}]	x, y	Cartesian coordinates [m]
h_p	Height of the porous layer [m]	X, Y	Non-dimensional Cartesian coordinates
H_p	Dimensionless height of the porous layer	α	Thermal diffusivity [$\text{m}^2 \text{s}^{-1}$]
k	Thermal conductivity [$\text{W m}^{-1} \text{K}^{-1}$]	β	Thermal expansion coefficient [K^{-1}]
K	Permeability of the porous media [m^2]	γ	Modified conductivity ratio
K_r	Wall to hybrid nanofluid thermal conductivity ratio	ε	Porosity of the medium
L	Non-dimensional length and height of the cavity	θ	Dimensionless temperature
N	Wavy wall wavenumber	μ	Dynamic viscosity [$\text{kg m}^{-1} \text{s}^{-1}$]
Nu_{av}	Overall average Nusselt number	ν	Kinematic viscosity [$\text{m}^2 \text{s}^{-1}$]
Nu_s	Local Nusselt number	ρ	Density [kg m^{-3}]
p	Pressure [N m^{-2}]	ϕ	Volume fraction of solids
P	Non-dimensional pressure	ψ	Stream function [$\text{m}^2 \text{s}^{-1}$]


References


- [1] Ismael, M.A., E. Abu-Nada, and A.J. Chamkha, Mixed convection in a square cavity filled with CuO-water nanofluid heated by corner heater, *International Journal of Mechanical Sciences*, 133, 2017, 42-50.
- [2] Geridonmez, B.P. and H.F. Oztop, Natural convection in a cavity filled with porous medium under the effect of a partial magnetic field, *International Journal of Mechanical Sciences*, 161, 2019, 105077.
- [3] Hussain, S.H., Analysis of heatlines and entropy generation during double-diffusive MHD natural convection within a tilted sinusoidal corrugated porous enclosure, *Engineering Science and Technology, an International Journal*, 19(2), 2016, 926-945.
- [4] Alsabery, A.I., et al., Impacts of amplitude and local thermal non-equilibrium design on natural convection within nanofluid superposed wavy porous layers, *Nanomaterials*, 11(5), 2021, 1277.
- [5] Rashidi, M., et al., New analytical method for the study of natural convection flow of a non-Newtonian fluid, *International Journal of Numerical Methods for Heat & Fluid Flow*, 2013.
- [6] Varol, Y. and H.F. Oztop, Free convection in a shallow wavy enclosure, *International Communications in Heat and Mass Transfer*, 33(6), 2006, 764-771.
- [7] Das, P.K. and S. Mahmud, Numerical investigation of natural convection inside a wavy enclosure, *International Journal of Thermal Sciences*, 42(4), 2003, 397-406.
- [8] Al-Srayyih, B.M., S. Gao, and S.H. Hussain, Effects of linearly heated left wall on natural convection within a superposed cavity filled with composite nanofluid-porous layers, *Advanced Powder Technology*, 30(1), 2019, 55-72.
- [9] Kadhim, H.T., et al., Numerical study of nanofluid flow in a square cavity with porous medium using a sinusoidal interface, 2019 4th Scientific International Conference Najaf (SICN), 2019, 216-221.
- [10] Nguyen, M.T., A.M. Aly, and S.-W. Lee, Effect of a wavy interface on the natural convection of a nanofluid in a cavity with a partially layered porous medium using the ISPH method, *Numerical Heat Transfer, Part A: Applications*, 72(1), 2017, 68-88.
- [11] Singh, A.K. and G.R. Thorpe, Natural convection in a confined fluid overlying a porous layer-a comparison, *Indian Journal of Pure and Applied Mathematics*, 26(1), 1995, 81-95.
- [12] Kasaean, A., et al., Nanofluid flow and heat transfer in porous media: A review of the latest developments, *International Journal of Heat and Mass Transfer*, 107, 2017, 778-791.
- [13] Miroshnichenko, I.V., et al., Natural convection of alumina-water nanofluid in an open cavity having multiple porous layers, *International Journal of Heat and Mass Transfer*, 125, 2018, 648-657.
- [14] Baytas, A.C. and I. Pop, Free convection in a square porous cavity using a thermal nonequilibrium model, *International Journal of Thermal Sciences*, 41(9), 2002, 861-870.
- [15] Khashan, S., et al., Numerical simulation of natural convection heat transfer in a porous cavity heated from below using a non-Darcian and thermal non-equilibrium model, *International Journal of Heat and Mass Transfer*, 49(5-6), 2006, 1039-1049.
- [16] Wu, F., et al., Buoyancy induced convection in a porous cavity with sinusoidally and partially thermally active sidewalls under local thermal non-equilibrium condition, *International Communications in Heat and Mass Transfer*, 75, 2016, 100-114.
- [17] Badruddin, I.A., et al., Numerical analysis of convection conduction and radiation using a non-equilibrium model in a square porous cavity, *International Journal of Thermal Sciences*, 46(1), 2007, 20-29.
- [18] Zargartalebi, H., et al., Unsteady free convection in a square porous cavity saturated with nanofluid: The case of local thermal nonequilibrium and Buongiorno's mathematical models, *Journal of Porous Media*, 20(11), 2017.
- [19] Feng, Y.-Y., et al., Internal thermal source effects on convection heat transfer in a two-dimensional porous medium: A lattice Boltzmann study, *International Journal of Thermal Sciences*, 173, 2022, 107416.
- [20] Wang, C.-H., et al., Numerical investigations of convection heat transfer in a thermal source-embedded porous medium via a lattice Boltzmann method, *Case Studies in Thermal Engineering*, 30, 2022, 101758.
- [21] Wang, C.-H., et al., Double-diffusive convection in a magnetic nanofluid-filled porous medium: Development and application of a nonorthogonal lattice Boltzmann model, *Physics of Fluids*, 34(6), 2022, 062012.
- [22] Wu, F., W. Zhou, and X. Ma, Natural convection in a porous rectangular enclosure with sinusoidal temperature distributions on both side walls using a thermal non-equilibrium model, *International Journal of Heat and Mass Transfer*, 85, 2015, 756-771.
- [23] Alsabery, A.I., et al., Impacts of amplitude and local thermal non-equilibrium design on natural convection within nanofluid superposed wavy porous layers, *Nanomaterials*, 11(5), 2021, 1277.
- [24] Izadi, M., et al., Nanoparticle migration and natural convection heat transfer of Cu-water nanofluid inside a porous undulant-wall enclosure using LTNE and two-phase model, *Journal of Molecular Liquids*, 261, 2018, 357-372.




- [25] Reddy, P.S. and P.J. Sreedevi, Entropy generation and heat transfer analysis of magnetic hybrid nanofluid inside a square cavity with thermal radiation, *The European Physical Journal Plus*, 136(1), 2021, 1-33.
- [26] Tayebi, T., et al., Natural convection and entropy production in hybrid nanofluid filled-annular elliptical cavity with internal heat generation or absorption, *Thermal Science and Engineering Progress*, 19, 2020, 100605.
- [27] Ashorynejad, H.R. and A.J.R. Shahriari, MHD natural convection of hybrid nanofluid in an open wavy cavity, *Results in Physics*, 9, 2018, 440-455.
- [28] Sheikholeslami, M., et al., Variable magnetic forces impact on magnetizable hybrid nanofluid heat transfer through a circular cavity, *Journal of Molecular Liquids*, 277, 2019, 388-396.
- [29] Chamkha, A.J., et al., Thermal non-equilibrium heat transfer modeling of hybrid nanofluids in a structure composed of the layers of solid and porous media and free nanofluids, *Energies*, 12(3), 2019, 541.
- [30] Ghalambaz, M., et al., Local thermal non-equilibrium analysis of conjugate free convection within a porous enclosure occupied with Ag-MgO hybrid nanofluid, *Journal of Thermal Analysis and Calorimetry*, 135(2), 2019, 1381-1398.
- [31] Alsabery, A.I., et al., Impact of two-phase hybrid nanofluid approach on mixed convection inside wavy lid-driven cavity having localized solid block, *Journal of Advanced Research*, 30, 2021, 63-74.
- [32] Gorla, R., et al., Heat source/sink effects on a hybrid nanofluid-filled porous cavity, *Journal of Thermophysics and Heat Transfer*, 31(4), 2017, 847-857.
- [33] Ghalambaz, M., et al., MHD natural convection of Cu-Al₂O₃ water hybrid nanofluids in a cavity equally divided into two parts by a vertical flexible partition membrane, *Journal of Thermal Analysis and Calorimetry*, 138(2), 2019, 1723-1743.
- [34] Izadi, M., et al., Natural convection of a magnetizable hybrid nanofluid inside a porous enclosure subjected to two variable magnetic fields, *International Journal of Mechanical Sciences*, 151, 2019, 154-169.
- [35] Selimefendigil, F. and H.F. Öztop, Conjugate natural convection in a cavity with a conductive partition and filled with different nanofluids on different sides of the partition, *Journal of Molecular Liquids*, 216, 2016, 67-77.
- [36] Chamkha, A.J., I.V. Miroschnichenko, and M.A. Sheremet, Numerical analysis of unsteady conjugate natural convection of hybrid water-based nanofluid in a semicircular cavity, *Journal of Thermal Science and Engineering Applications*, 9(4), 2017, 041004.
- [37] Sahoo, R.R., P. Ghosh, and J. Sarkar, Performance analysis of a louvered fin automotive radiator using hybrid nanofluid as coolant, *Heat Transfer—Asian Research*, 46(7), 2017, 978-995.
- [38] Mehryan, S.A., et al., Free convection of hybrid Al₂O₃-Cu water nanofluid in a differentially heated porous cavity, *Advanced Powder Technology*, 28(9), 2017, 2295-2305.
- [39] Kadhim, H.T., E.A. Jabbar, and A. Rona, Cu-Al₂O₃ hybrid nanofluid natural convection in an inclined enclosure with wavy walls partially layered by porous medium, *International Journal of Mechanical Sciences*, 186, 2020, 105889.
- [40] Takabi, B. and S. Salehi, Augmentation of the heat transfer performance of a sinusoidal corrugated enclosure by employing hybrid nanofluid, *Advances in Mechanical Engineering*, 6, 2014, 147059.
- [41] Hussein, A.K. and S.H. Hussain, Heatline visualization of natural convection heat transfer in an inclined wavy cavities filled with nanofluids and subjected to a discrete isoflux heating from its left sidewall, *Alexandria Engineering Journal*, 55(1), 2016, 169-186.
- [42] Suresh, S., et al., Synthesis of Al₂O₃-Cu/water hybrid nanofluids using two step method and its thermo physical properties, *Colloids and Surfaces A: Physicochemical and Engineering Aspects*, 388(1-3), 2011, 41-48.
- [43] Chamkha, A.J. and M.A. Ismael, Natural convection in differentially heated partially porous layered cavities filled with a nanofluid, *Numerical Heat Transfer, Part A: Applications*, 65(11), 2014, 1089-1113.
- [44] Khanafer, K., K. Vafai, and M. Lightstone, Buoyancy-driven heat transfer enhancement in a two-dimensional enclosure utilizing nanofluids, *International Journal of Heat and Mass Transfer*, 46(19), 2003, 3639-3653.
- [45] Alsabery, A., et al., Effects of nonuniform heating and wall conduction on natural convection in a square porous cavity using LTNE model, *Journal of Heat and Mass Transfer*, 139(12), 2017, 122008.
- [46] Basak, T., et al., Natural convection in a square cavity filled with a porous medium: effects of various thermal boundary conditions, *International Journal of Heat and Mass Transfer*, 49(7-8), 2006, 1430-1441.
- [47] Basak, T., et al., Finite element based heatline approach to study mixed convection in a porous square cavity with various wall thermal boundary conditions, *International Journal of Heat and Mass Transfer*, 54(9-10), 2011, 1706-1727.
- [48] Abu-Nada, E. and A.J. Chamkha, Effect of nanofluid variable properties on natural convection in enclosures filled with a CuO-EG-water nanofluid, *International Journal of Thermal Sciences*, 49(12), 2010, 2339-2352.
- [49] Brinkman, H., The viscosity of concentrated suspensions and solutions, *The Journal of Chemical Physics*, 20(4), 1952, 571-571.
- [50] Aminossadati, S. and B. Ghasemi, Natural convection cooling of a localised heat source at the bottom of a nanofluid-filled enclosure, *European Journal of Mechanics-B/Fluids*, 28(5), 2009, 630-640.
- [51] Donea, J. and A. Huerta, *Finite element methods for flow problems*, John Wiley & Sons, 2003.
- [52] Nithiarasu, P., R.W. Lewis, and K.N. Seetharamu, *Fundamentals of the finite element method for heat and mass transfer*, John Wiley & Sons, 2016.
- [53] Chen, Y. and X. Zhang, A P2-P1 partially penalized immersed finite element method for Stokes interface problems, *International Journal of Numerical Analysis and Modeling*, 18(1), 2021.
- [54] Hauke, G. and T. Hughes, A unified approach to compressible and incompressible flows, *Computer Methods in Applied Mechanics and Engineering*, 113(3-4), 1994, 389-395.
- [55] COMSOL, M., *Comsol multiphysics user guide (version 5.2)*, COMSOL, AB, 2015.
- [56] Roache, P.J., *Perspective: a method for uniform reporting of grid refinement studies*, 1994.
- [57] Wilcox, D.C., *Turbulence modeling for CFD*, La Canada, CA: DCW Industries, 2006.
- [58] Baytas, A.J.I., Thermal non-equilibrium natural convection in a square enclosure filled with a heat-generating solid phase, non-Darcy porous medium, *International Journal of Energy Research*, 27(10), 2003, 975-988.
- [59] Beckermann, C., S. Ramadhyani, and R. Viskanta, Natural convection flow and heat transfer between a fluid layer and a porous layer inside a rectangular enclosure, *ASME Journal of Heat and Mass Transfer*, 109(2), 1987, 363-370.
- [60] Wang, L., et al., Effects of temperature-dependent viscosity on natural convection in a porous cavity with a circular cylinder under local thermal non-equilibrium condition, *International Journal of Thermal Sciences*, 159, 2021, 106570.
- [61] Ali, A.M., et al., Thermo-hydraulic performance of a circular microchannel heat sink using swirl flow and nanofluid, *Applied Thermal Engineering*, 191, 2021, 116817.
- [62] Alsabery, A.I., et al., Effect of local thermal non-equilibrium model on natural convection in a nanofluid-filled wavy-walled porous cavity containing inner solid cylinder, *Chemical Engineering Science*, 201, 2019, 247-263.
- [63] Zhang, L., Y. Hu, and M. Li, Numerical study of natural convection heat transfer in a porous annulus filled with a Cu-nanofluid, *Nanomaterials*, 11(04), 2021, 990.
- [64] Shafiee, H., E. NikzadehAbbasi, and M. Soltani, Numerical study of the effect of magnetic field on nanofluid heat transfer in metal foam environment, *Geofluids*, 2021, 2021, 3209855.

ORCID iD

Hakim T. Kadhim  <https://orcid.org/0000-0002-2397-7821>

Zaid M. Al Dulaimi  <https://orcid.org/0000-0001-5697-5753>

Aldo Rona  <https://orcid.org/0000-0001-5866-9776>



© 2022 Shahid Chamran University of Ahvaz, Ahvaz, Iran. This article is an open access article distributed under the terms and conditions of the Creative Commons Attribution-NonCommercial 4.0 International (CC BY-NC 4.0 license) (<http://creativecommons.org/licenses/by-nc/4.0/>).



How to cite this article: Kadhim H.T., Al Dulaimi Z.M., Rona A. Local Thermal Non-equilibrium Analysis of Cu-Al₂O₃ Hybrid Nanofluid Natural Convection in a Partially Layered Porous Enclosure with Wavy Walls, *J. Appl. Comput. Mech.*, 9(3), 2023, 712–727. <https://doi.org/10.22055/jacm.2022.42046.3863>

Publisher's Note Shahid Chamran University of Ahvaz remains neutral with regard to jurisdictional claims in published maps and institutional affiliations.

